Geophys. J. Int. (2007) **170,** 1165–1179 doi: 10.1111/j.1365-246X.2007.03415.x

Multi-interferogram method for measuring interseismic deformation: Denali Fault, Alaska

Juliet Biggs,[1] Tim Wright,[2] Zhong Lu[3] and Barry Parsons[1]

[1] *COMET, Department of Earth Sciences, University of Oxford. Parks Road, Oxford,* OX1 3PR, *UK*
[2] *School of Earth and the Environment, Environment Building, University of Leeds, Leeds,* LS2 9JT, *UK*
[3] *US Geological Survey, Earth Resources Observation and Science Center,* 47914 252nd *Street, Sioux Falls, South Dakota, USA*

Accepted 2007 February 21. Received 2007 February 20; in original form 2006 September 27

SUMMARY

Studies of interseismic strain accumulation are crucial to our understanding of continental deformation, the earthquake cycle and seismic hazard. By mapping small amounts of ground deformation over large spatial areas, InSAR has the potential to produce continental-scale maps of strain accumulation on active faults. However, most InSAR studies to date have focused on areas where the coherence is relatively good (e.g. California, Tibet and Turkey) and most analysis techniques (stacking, small baseline subset algorithm, permanent scatterers, etc.) only include information from pixels which are coherent throughout the time-span of the study. In some areas, such as Alaska, where the deformation rate is small and coherence very variable, it is necessary to include information from pixels which are coherent in some but not all interferograms. We use a three-stage iterative algorithm based on distributed scatterer interferometry. We validate our method using synthetic data created using realistic parameters from a test site on the Denali Fault, Alaska, and present a preliminary result of 10.5 ± 5.0 mm yr^{-1} for the slip rate on the Denali Fault based on a single track of radar data from ERS1/2.

Key words: continental deformation, fault slip, satellite geodesy.

1 INTRODUCTION

Previous studies have clearly demonstrated the potential of InSAR to detect and measure slow tectonic signals such as interseismic strain accumulation in places with good interferometric conditions (e.g. Wright *et al.* 2001). However, in the long term, InSAR may have the potential to produce continental scale fault maps which identify all active structures and measure the rate of strain accumulation across them. Such a map would be a crucial tool for hazard assessment and provide a valuable data set to advance our understanding of the mechanics of continental deformation. In order to achieve this, it is necessary to extend the range of study areas to places with less ideal conditions. A dedicated InSAR satellite would provide a much larger volume of data than is currently routinely available and it is important to understand how this can be used to combat the problems of interferometric decorrelation.

In comparison with other geophysical phenomena studied using InSAR, interseismic strain accumulation is small in magnitude and spread over large spatial distances and temporal time-spans. Interseismic slip rates on major plate boundary faults, such as the North Anatolian and San Andreas Faults, are typically up to 40 mm yr^{-1}. However, for intra-continental faults, slip rates of 1–2 mm yr^{-1} are more typical. The Denali Fault, Alaska, has an intermediate slip rate, difficult interferometric conditions, but a large archive of available data. These are conditions which we might expect if attempting to produce a global map of fault deformation using a dedicated InSAR satellite.

Current analysis techniques, such as stacking (e.g. Wright *et al.* 2001), permanent scatterers (Ferretti *et al.* 2000) and SBAS (Berardino *et al.* 2002), rely on pixels or points being coherent throughout the data set. Outside dry, rocky and urban areas, these conditions are rarely met. As an example, we use data covering the Denali Fault collected by European Space Agency's ERS satellites and the Alaska SAR Facility (ASF). Despite an excellent archive of data acquisitions, the distributed scatterer interferograms are not consistently coherent enough that it is possible to construct a subset which covers both sufficient area and sufficient time to detect interseismic strain. We find it necessary to modify existing analysis techniques in order to include information from pixels which are only coherent in some of the interferograms.

1.1 Tectonic background: the Denali Fault, Alaska

The tectonics of Alaska are controlled by the interaction between the Pacific and North American Plates. Both the rate of convergence and nature of the interface changes along the plate boundary. In the west, the Pacific Plate is subducting under the North American Plate at a rate of 68 mm yr^{-1}. To the east, the Queen Charlotte Transform is a transpressive strike-slip fault. Linking these two contrasting styles of plate boundary is a complex region of continental deformation

© 2007 The Authors
Journal compilation © 2007 RAS

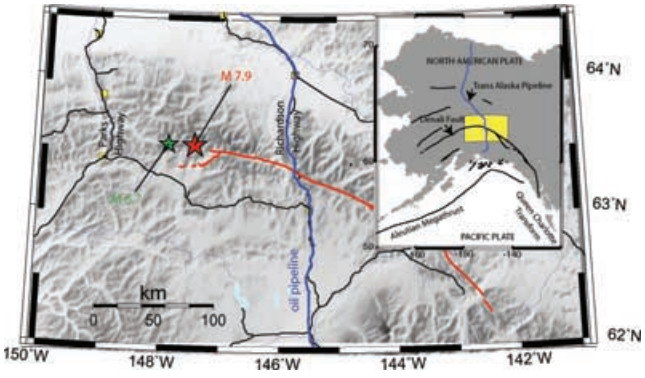

Figure 1. (a) Location map showing the Pacific–North American Plate boundary in Alaska. The Denali Fault is part of a complex zone of continental deformation between the Aleutian megathrust and the Queen Charlotte Transform. (b) 2002 Denali Earthquake Sequence showing location of M6.7 Nenana Mountain Earthquake and M7.9 Denali Fault Earthquake and associated aftershocks (after Fuis & Wald 2003).

extending several hundred kilometres inland through southern Alaska (Fig. 1). The Denali Fault is one of the most dominant topographic features within this zone, extending for over a thousand kilometres through Alaska and into Canada.

The M_w 7.9, 2002 November 3, Denali Earthquake was the largest strike-slip earthquake in North America for more than 150 yr (Fig. 1). The total rupture length was 340 km with offsets of up to 9 m (Eberhart-Phillips *et al.* 2003). The earthquake began with thrust motion on the previously unrecognized Susitna Glacier Fault and then ruptured unilaterally from west to east with right-lateral slip along the Denali and then Totshunda Faults (Wright *et al.* 2004a; Hreinsdottir *et al.* 2006). Only 10 days earlier on 2002 October 23, the M_w 6.7 Nenana Mountain Earthquake occurred further west on the Denali Fault, significantly increasing the Coulomb stress at the hypocenter of the M_w 7.9 November earthquake (Anderson & Ji 2003). Prior to the 2002 earthquake sequence, a magnitude M_w 7.2 earthquake is believed to have ruptured at least part of the same segment of the Denali Fault in 1912 (Carver *et al.* 2004; Doser 2004). Between 1912 and 2002 the level of recorded seismicity on this section of the Denali Fault was very low with the majority of earthquakes $M > 4.5$ occurring on thrust faults to the north or south (Doser 2004).

Previous estimates of the slip rate on the Denali Fault are variable, ranging from $\leq$3 to 10–20 mm yr^{-1} (Table 1). The scatter of measurements is likely to be due to variations in slip rate along strike and the assumptions used in the different techniques, some geodetic and some geological. The offset features measured in the studies of Stout *et al.* (1973), Hickman *et al.* (1977) and Plafker *et al.* (1994) are assumed to have an age of 11 000 yr, but no specific dating has been done on these features. The study of Matmon *et al.* (2006) uses ^{10}Be exposure age dating of boulders and sediments from offset moraines to estimate slip rates at a number of sites along the Denali and Totshunda Faults. They find a decrease in slip rate from east (14.4 ± 2.5 mm yr^{-1}) to west (9.4 ± 1.6 mm yr^{-1}) along the Denali fault. This decrease has been attributed to the curvature of the Denali Fault which causes an associated increase in shortening across the fault, as expressed by the broad zone of folding and thrusting in the northern foothills and partitioning of slip onto other active structures. Alternative studies of postglacial slip rates find an even stronger decrease from a rate of 13 mm yr^{-1} at 144° W to 7 mm yr^{-1} at 149° W (Meriaux *et al.* 2004).

Networks of triangulation points or GPS stations can be used to produce a geodetic estimate of slip rate using a deep-fault model of interseismic deformation in which the fault extends from the surface to infinite depth as a single discrete plane (Savage & Burford 1973; Prescott & Nur 1981). In the seismogenic layer, the fault behaves in a stick-slip manner; earthquakes occur as discrete events and no motion takes place on the fault for the remainder of the earthquake cycle. Beneath the seismogenic layer, the fault creeps continuously and the surrounding material behaves elastically. The seismogenic layer acts as an elastic lid, which responds passively to the deformation in the lower layer. This situation can be represented as a screw dislocation extending from the base of the seismogenic layer to great depth within an elastic half-space. The rate of fault-parallel surface displacement, y, at a perpendicular distance x from the fault with locking depth d and slip rate s is given by

$$y = \frac{s}{\pi} \tan^{-1} \frac{x}{d}. \quad (1)$$

A profile of fault parallel deformation can then be interpreted to find locking depth and slip rate. The triangulation networks of Page & Lahr (1971) and Savage & Lisowski (1991) only include stations within 20 km of the fault. The absence of any true far field sites makes the trade-offs between locking depth and slip rate difficult to assess. The GPS data of Fletcher (2002) can be fit with a variety of models, but some evidence is found for a second structure accumulating strain ~35 km north of the Denali Fault.

Table 1. Previous estimates of slip rates on the Denali Fault from geomorphology and geodesy. Several possible interpretations of the GPS data of Fletcher (2002) give a range of possible values. In general, the geodetic estimates are lower than those from geomorphology.

Method	Estimate (mm yr^{-1})	Reference
Holocene offsets	8–12	Plafker *et al.* (1994)
Holocene offsets (nr Richardson Highway)	4.5–5.5	Stout *et al.* (1973)
Holocene OFFSETS (nr Parks Highway)	10–21	Hickman *et al.* (1977)
Late Pleistocene–Holocene offsets (central Denali)	12.0 ± 1.7	Matmon *et al.* (2006)
Triangulation network (1975–1988)	$\leq$5	Savage & Lisowski (1991)
Triangulation network (1967–1969)	$\leq$3	Page & Lahr (1971)
VLBI	$\leq$5	Ma *et al.* (1990)
GPS (Single Fault Model)	8 ± 1	Fletcher (2002)
GPS (Two Fault Model)	[a]5 ± 2	Fletcher (2002)
GPS (Block Rotation Model	6	Fletcher (2002)
GPS (Two Fault Block Rotation Model)	5	Fletcher (2002)
InSAR	11.8 ± 5.0	This study

[a]Multifault model applies to the Parks Highway profile (west of this study area) and accommodates an additional 3 mm yr^{-1} on parallel strand within the same fault system.

Outline

In this paper, we begin by analysing a set of individual interferograms constructed over the Denali Fault in terms of their tectonic, orbital and atmospheric contributions, coherence and unwrapping errors. This understanding allows us to create a set of synthetic data with similar characteristics, but a known slip rate. We test various existing algorithms based on stacking and time-series approaches but find none of them are applicable to this particular problem. We develop a new technique combining a network orbital correction, construction of a rate map and an inversion to find the slip rate. We demonstrate the method accurately reproduces known slip rates in synthetic tests and apply it to the Denali Fault, where a slip rate of 10.5 $\pm$ 5.0 mm yr^{-1} is found.

2 ANALYSIS OF PHASE CONTRIBUTIONS TO INDIVIDUAL INTERFEROGRAMS

The Alaska SAR Facility (ASF) has an extensive archive of SAR data over Alaska collected using the European Space Agency's satellites ERS-1 and ERS-2. We chose to study the Denali Fault at the point where the Alaska Range is crossed by the Trans-Alaska Pipeline and Richardson Highway (Fig. 1) where coseismic studies have demonstrated better coherence (Wright *et al.* 2004a). Of the six tracks which cover this area, three ascending and three descending, we use descending track 329 as a test track. During the mainly snow-free months of March–November in the years between 1992 (the launch of ERS-1) and 2002 (the Denali Earthquake) there were 48 acquisitions (Fig. 2). Interferograms are processed using the JPL/Caltech ROI_PAC software (Rosen *et al.* 2004), filtered using a power spectrum filter (Goldstein & Werner 1998) and unwrapped using a branch cut algorithm (Goldstein *et al.* 1988). We use the resulting data set to investigate the characteristics of orbital and atmospheric errors and coherence in the Denali Region. Some examples showing typical orbital and atmospheric errors and the results for various combinations of temporal and spatial baseline are shown in Fig. 3.

2.1 Coherence

In order to construct an interferogram, the phase response from a pixel on the ground must remain roughly constant between the two image acquisitions. This factor is usually quantified in terms of

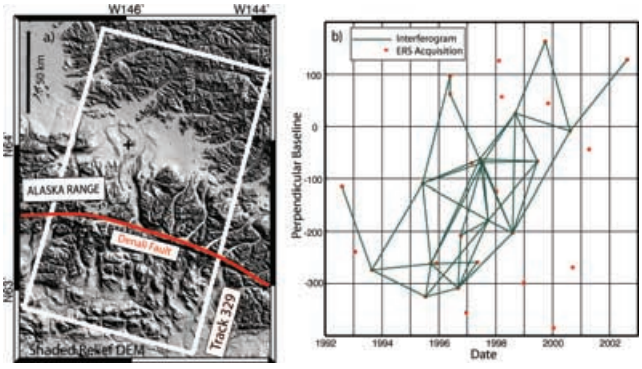

Figure 2. Baseline-time plot for descending track 329 showing acquisitions between March and November only. Solid lines represent interferograms where unwrapping across the Alaska Range was possible; these interferograms form the basis for this study.

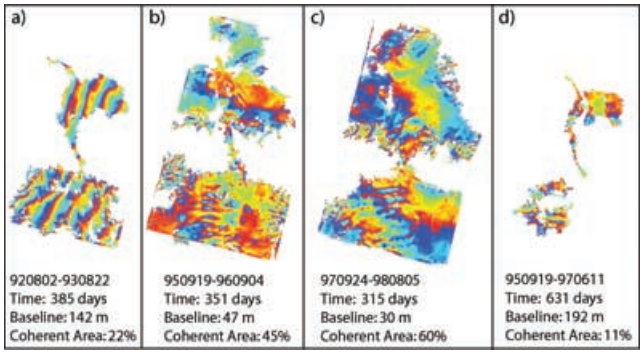

Figure 3. Example interferograms from Denali Fault Data set. (a) Example with large residual orbital error equivalent to 6 fringes across-track. (b) Example with significant short-wavelength water-vapour related features (likely to be caused by gravity waves) (c) Shorter duration, shorter baseline interferogram showing high coherence (d) Long duration, long baseline interferogram showing poor coherence; although in this case it was possible to unwrap manually across the Alaska Range.

interferometric correlation, γ, across a 3 $\times$ 3 pixel window, where $\gamma = 1$ for perfectly stable pixels and $\gamma = 0$ if the phase response in the two images is independent. We chose a coherence threshold of $\gamma =$ 0.15. Regions composed of pixels whose γ is above this threshold typically produce a smooth field when unwrapped and thus these pixels are considered 'coherent' whereas pixels for which γ is less than this threshold appear to have random phase values. We expect the percentage of coherent pixels in an interferogram to decrease with both temporal and spatial baseline (Fig. 4).

The topographic contribution to an interferogram results from the difference in incidence angles between the two acquisitions and so scales with both topography and perpendicular baseline. For steep slopes and/or large baselines, the phase difference across a single pixel may be large enough to cause geometric decorrelation. Temporal decorrelation occurs when the properties or distribution of radar scatterers within a pixel changes between acquisitions. Stable surfaces, such as urban and dry, rocky areas remain coherent for many years whereas very unstable surfaces, typically dense vegetation, may lose coherence in a few days.

For the Denali region, there is considerable variation in the percentage of coherent pixels in an interferogram with any given baseline combination (see Table S1 in the Supplementary Material, available in the online version of the journal), but the maximum achievable percentage decays rapidly with both temporal and spatial baseline. For interferograms of duration $\sim$1 yr, up to $\sim$60 per cent of pixels may be coherent, but for interferograms with duration $\sim$2 yr, this is reduced to only $\sim$25 per cent (Fig. 4).

However, it is not just the total number of coherent pixels which is important, but the number of pixels whose phase can be unwrapped relative to a reference pixel. Like many other major strike-slip faults, the Denali fault is associated with a significant topographic feature; the Alaska Range with relief in excess of 4 km. The steep slopes of the Alaska Range cause geometric decorrelation and provide a barrier to unwrapping. For this reason, we focus our study on the area around the Delta River Valley which crosses the Alaska Range and contains the Trans-Alaska Pipeline and the Richardson Highway. In many cases, this valley provides a coherent bridge between the lowland areas to the north and to the south. From the 48 acquisitions on the chosen track, it is possible to construct 77 interferograms with duration $<$2 yr and perpendicular baseline $<$200 m. Of these, 44 could be unwrapped across the fault and these interferograms form the basis for this study (Fig. 2).

© 2007 The Authors, *GJI*, **170,** 1165–1179
Journal compilation © 2007 RAS

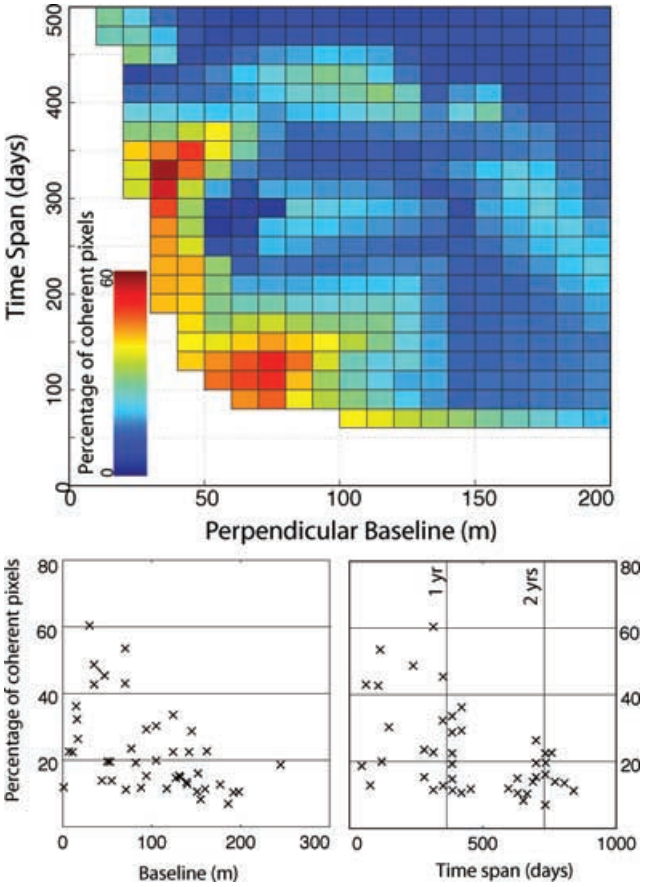

Figure 4. Decrease in percentage of coherent pixels in an interferogram with both spatial and temporal baseline. (a) Data are interpolated onto a grid of 10 m × 20 days using triangle-based linear interpolation (b) variation with spatial baseline c) variation with temporal baseline. Pixels are defined as coherent if $\gamma > 0.15$. For interferograms of duration ∼1 yr up to ∼60 per cent of pixels may be coherent, but for interferograms with duration ∼2 yr, this is reduced to only ∼25 per cent.

2.2 Contribution from interseismic strain accummulation

Interseismic strain accumulation occurs slowly in comparison to other types of tectonic signal traditionally studied using InSAR, such as coseismic deformation. We wish to predict the approximate contribution of interseismic deformation to a single interferogram using previous estimates of slip rate on the Denali Fault.

We use the deep fault model described in Section 1.1 for which the locking depth is equivalent to the thickness of the seismogenic layer which can be inferred from studies of coseismic deformation. Distributed slip models of coseismic deformation based on geodetic data from the 2002 Denali Fault earthquake find the majority of slip occurred at depth above 12–15 km (Hreinsdottir *et al.* 2003; Wright *et al.* 2004a; Hreinsdottir *et al.* 2006). However, there was a patch of slightly deeper slip in the area of the Trans-Alaska Pipeline, which suggest a thicker seismogenic layer may be appropriate for this study.

The Denali Fault has significant curvature and for modelling purposes has often been approximated by a small circle bounding a rotating block with the pole of rotation located near the southern coast of Alaska (Stout & Chase 1980; Fletcher 2002; Freed *et al.* 2006). However, for this study we focus on a short segment (<100 km) so chose to model the fault as linear feature for simplicity. This may result in some inaccuracies in the area near the fault.

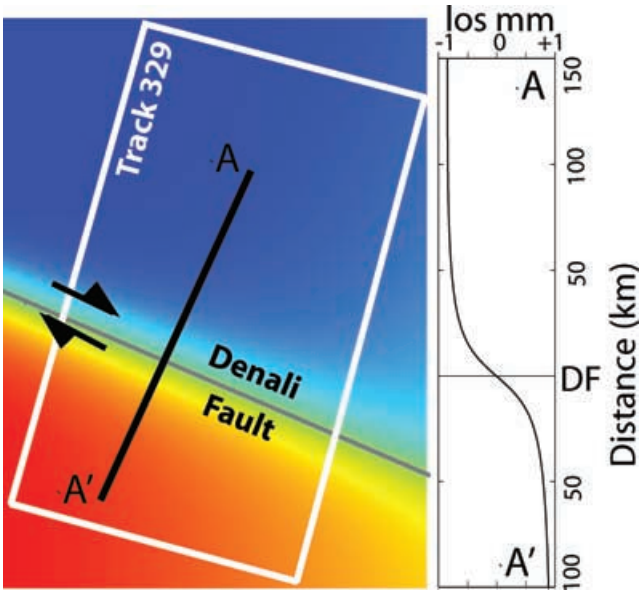

Figure 5. Model interferogram based on a deep fault model with a locking depth of 15 km and a slip rate of 5 mm yr^{-1}. The fault-parallel motion over a 1 year duration are projected into the satellite line-of-sight (los) for a descending orbit taking into account variations of incidence angle across track. Blue colours represent range decrease and red represents range increase.

Fig. 5 shows the predicted deformation over a period of 1 yr for a deep fault model moving at 5 mm yr^{-1} below an elastic lid 15 km thick. The deformation is projected into the satellite line-of-sight appropriate for the interferograms used in this study. The values vary between ±0.9 mm with a maximum gradient of 0.04 mm km^{-1}. This is significantly less than the 28 mm of range change required to produce a single interference fringe.

2.3 Orbital contribution

Satellites are perturbed from a nominal elliptical orbit by a number of phenomena. Some, such as tidal pull and lateral variations in the earth's gravity field can be modelled accurately, but others including solar radiation pressure, thermal reradiation and atmospheric drag are more difficult to predict (Ziebart *et al.* 2005). Through orbital manoeuvres, the ERS satellites are steered to ±1 km of the nominal ground track. As a result, the two radar images which are combined to create an interferogram are usually taken from different locations. This baseline separation causes a difference in path length which varies primarily with incidence angle and to a lesser degree with topography. InSAR processing software, such as ROI_PAC, initially removes the effect of baseline separation approximating the surface of the earth to be a smooth ellipsoid; once linearized, the resulting rate of change in phase with respect to incidence angle is directly proportional to the perpendicular baseline. Subsequently, a digital elevation model (DEM) can be use to correct for additional topographic effects.

Our knowledge of the satellite orbits is imperfect: the best available models for ERS have quoted accuracies of 5–7 cm radially and 10–15 cm cross-track (Scharoo & Visser 1998). Therefore, even after the effects of baseline separation have been removed, an orbital error remains in the interferogram (Fig. 3a) (Zebker *et al.* 1994). The orbital parameters can be re-estimated empirically following filtering and unwrapping by finding the perturbation to the orbital parameters which best matches the observed phase. Since the

unmodelled accelerations are usually small, the baseline error changes slowly in the along track direction. For short strips of data (i.e. 1–2 frames, 100–200 km along track) a linear approximation is usually sufficiently accurate, but for longer strips of data, a quadratic approximation may be required. Hanssen (2001) finds that the ratio between the coefficient of the quadratic term and the linear term is approximately 10^{-6} indicating the signal is only weakly curved.

Attempting to remove the orbital contribution empirically will also remove the long-wavelength component of the signal. For many applications, such as glaciology and volcanology, this approach is sufficient since the deformation signal is only present in a small portion of the interferogram (e.g. Pritchard & Simons 2002; Rignot 1998) and it is possible to define a 'far-field' area of the interferogram which is not affected by deformation and use this to re-estimate the baseline parameters. However, for studies of interseismic deformation the signal covers such a large area that there is no true 'far-field'. For this reason, we prefer not to re-estimate the baseline for individual interferograms during processing and to deal with the issue of orbital contributions at a later stage.

However, we wish to understand the nature of the orbital errors, so we perform simple tests assuming that in individual interferograms, the interseismic deformation is negligible and that atmospheric errors are short-wavelength in comparison to orbital errors. We approximate the contribution from the orbital error to be planar and find the best-fitting plane to each interferogram, $z = ux + vy + w$, where $[x, y]$ is the pixel coordinate (in surface UTM coordinates), u and v are gradient parameters and w is the intercept. We find that both x- and y-gradients have a roughly normal distribution centred on zero (see Fig. S2 in the Supplementary Material). This confirms that the orbital errors can be assumed to be random, that is, there is no systematic bias, and that the long-wavelength tectonic signal is much smaller than the contribution from orbital errors. The mean absolute y-gradient is 0.19 mm km^{-1}, a factor of five greater than the maximum gradient from our synthetic 1-yr interferogram for interseismic deformation (0.04 mm km^{-1}). It is interesting to note that this mean absolute y-gradient is equivalent to about 1.5 fringes across a single frame measuring 100 × 100 km whereas Hanssen (2001) predicts significantly less than a fringe for the stated along-track and radial errors. It appears this estimation/correction technique also accounts for other long wavelength signals, such as ionspheric and long wavelength tropospheric contributions as well as errors in orbit.

2.4 Atmospheric contribution

Atmospheric errors result from interactions between the radar beam and the atmosphere it passes through (e.g. Fig. 3b). The amount of atmospheric phase delay is determined by the refractive index; primarily a function of pressure and temperature (the 'dry' component) and water-vapour content (the 'wet' component). On the length-scale of interferograms, the most variable, and therefore, the most significant factor is the amount of water vapour in the troposphere. By fitting a 1-D covariance function to each of the interferograms, we investigate the magnitude and spatial scale of the atmospheric errors in our test area (Fig. 6). To simplify the analysis, we assume that the statistical properties of the water vapour field are radially symmetric and have a homogeneous structure across the interferogram (Hanssen 2001; Parsons *et al.* 2006) — an assumption that breaks down in certain atmospheric situations such as the presence of a weather front. The key statistical characteristics of the contribution of the water vapour field to an interferogram can then be fully described using a 1-D covariance function. The 1-D covariance

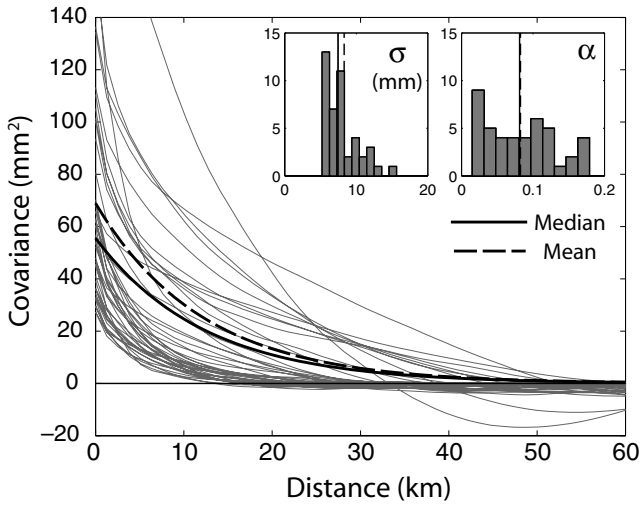

Figure 6. 1-D covariance functions for the Denali interferograms — functions are averaged azimuthally and binned every 1.2 km. Insets show distribution of covariance parameters σ and α with mean and median values. Bold lines show parametrized 1-D variance functions using mean and median values.

function can then be parametrized using a suitable functional form, for example, $c_{jk} = \sigma^2 e^{(-d_{jk}/\alpha)}$, where c_{jk} is the covariance between pixels j and k, σ^2 is the variance, α is the e-folding wavelength and d_{jk} is the distance between pixels. More complicated functional forms can be used which allow negative values of covariance, however, we chose this form for the sake of simplicity. We find median values of $\sigma = 7.5$ mm and $\alpha = 12.3$ km. This compares well with previous estimates of atmospheric noise based on simple statistical tests. For example, Hanssen (2001), reports root mean square (rms) values attributed to atmospheric errors ranging from 2.2 to 15.6 mm for a set of 26 interferograms over the Netherlands; Lyons & Sandwell (2003) find standard deviations ranging from 0.98 to 13.45 mm, with a median of 8.13 mm for a set of 46 interferograms from California. These values are all much larger than the predicted range change of 2 mm caused by interseismic deformation in a single, 1-yr interferogram.

2.5 Unwrapping errors

The phase values in an interferogram are initially wrapped modulo 2π and an unwrapping step during processing attempts to remove the 2π ambiguity to produce a continuous map of phase values. For complete spatial coverage and in the absence of noise, this is a simple process. Various algorithms, such as branch cut (Goldstein *et al.* 1988) and minimum cost flow (Chen & Zebker 2000) have been developed to tackle this problem in a range of conditions. Nevertheless, the resulting interferogram often has unwrapping errors which appear as 2π phase jumps which can be spotted visually and manually corrected.

The currently available unwrapping algorithms use spatial information from a single interferogram. If a large data set is being produced, including multiple interferograms constructed using common master or slave images, then additional constraints could be included by unwrapping the data set as a whole. Such a 3-D approach has already been developed for persistent scatterer interferometry (Hooper & Zebker, in preparation). Developing such an algorithm for distributed scatterer interferometry is beyond the scope of this paper, but we use constraints from a network of interferograms to

© 2007 The Authors, *GJI*, **170,** 1165–1179
Journal compilation © 2007 RAS

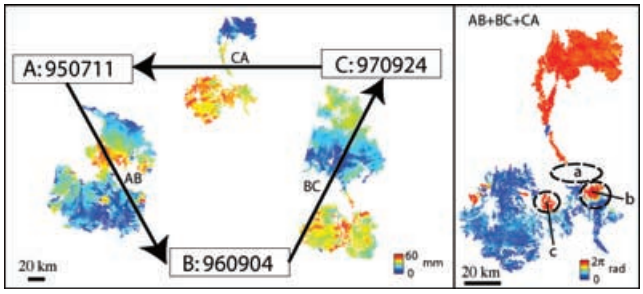

Figure 7. Phase closure. The tectonic, orbital and atmospheric contributions to an interferogram should be conservative. Unwrapping errors are not conservative and can be identified by summing round a loop. Phase jumps, shown by a colour change blue to red, correspond to unwrapping errors in one or more interferogram. In this case, the phase jump in the region labelled 'a' could be attributed to either interferogram AC or BC, and the phase jumps labelled 'b' and 'c' can be attributed to unwrapping errors in interferograms BC and AB, respectively.

identify unwrapping errors remaining after using the more traditional branch-cut unwrapping algorithm.

The phase contributions discussed so far, (tectonic, orbital and atmospheric) behave in a conservative manner. That is $\phi_{ln} - \phi_{lm} - \phi_{mn} = 0$, where ϕ_{lm} is the phase contribution to interferogram lm which is constructed from acquisitions l and m. Unwrapping errors will not follow this rule so can be identified by summing round a loop, and looking for residuals. Fig. 7 shows several such unwrapping errors, labelled 'a','b' and 'c', which are identified as 2π phase jumps (blue–red). In order to identify the source of the unwrapping error, each interferogram must be inspected individually. Finding the exact location of the phase jump is further complicated since the loop can only be constructed for pixels which are coherent in all three interferograms. In the example shown in Fig. 7 there is clearly an unwrapping error somewhere in the region marked 'a', but since both interferograms AC and BC have gaps in coherence at this location, it is not obvious which interferogram should be corrected. In this case, it is necessary to go back and check both interferograms at the stage before unwrapping, and in some cases, before filtering to identify the error. Several smaller unwrapping errors can be seen in Fig. 7 and the source of these errors is usually simpler to identify—in this case the errors labelled 'b' and 'c' can be seen in interferograms BC and AB, respectively.

Ideally this technique could be used to automatically detect and correct all unwrapping errors. However, in practice, for a large network of interferograms, the number of small unwrapping errors combined with non-discrete errors caused by filtering and resampling makes this difficult to implement automatically and time-consuming to implement manually. As a result, we restrict ourselves to identifying major unwrapping errors, paying particular attention to the area around the fault so that even the 'corrected' data set contains a large number of small unwrapping errors.

3 EXISTING METHODS

We have demonstrated that the atmospheric and orbital contributions to a 1-yr interferogram are many times larger than the predicted contribution from interseismic deformation along the Denali Fault. In addition, the duration of an interferogram is limited by temporal decorrelation so that it is not possible for an individual interferogram to cover a sufficiently long-time period such that the interseismic deformation accumulated is greater than the noise.

3.1 Stacking

Several methods have been used to combine multiple interferograms to combat this problem. The simplest, stacking, works on the principle that the signal in the interferograms has a systematic pattern, while the atmospheric noise is random. Addition of N interferograms with equal duration has a signal N times larger than a single interferogram, but the noise is only $\sqrt{N}$ times larger. The signal-to-noise ratio is improved by a factor of $\sqrt{N}$. This method has been used to detect and measure interseismic strain accumulation in Turkey (Wright *et al.* 2001), California, (Peltzer *et al.* 2001; Fialko 2006) and Tibet, (Wright *et al.* 2004b).

Most previous studies using stacking have been carried out in areas of good coherence and only pixels which are coherent in all interferograms are used. However, for the Denali data set, the permanently coherent pixels do not cover a sufficiently large area for observations of interseismic deformation to be possible. An alternative approach would be to discard the least coherent interferograms, to form a smaller, but more coherent data set. By ranking the interferograms according to the percentage of coherent pixels and successively adding them to the stack, we investigate the spatial coverage possible for a variety of stacks. We find that stacks which include a large number of interferograms and so cover a long duration do not have sufficient commonly coherent pixels. Conversely, any stack with sufficient spatial coverage, does not have sufficient duration for the interseismic signal to exceed the atmospheric noise (Fig. 8).

3.2 Chain stacking

The atmospheric and orbital contributions to an interferogram can be split into master and slave components. The stacking method can be improved by constructing a chain of interferograms, such that the slave of one interferogram is the master of the next. The orbital and atmospheric contributions from acquisitions in the middle of

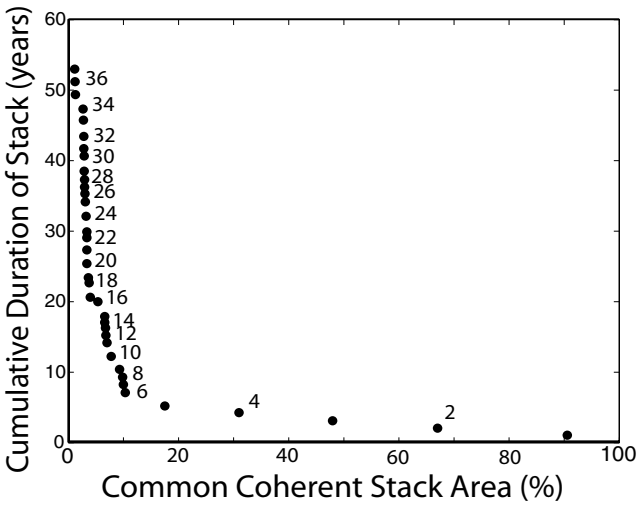

Figure 8. Plot showing spatial and temporal coverage for a range of possible inteferogram stacks. The interferograms are added to the stack in order, starting with the most coherent. Percentage areas are calculated with a pixel size of 640m. After adding each interferogram, the resulting stack time-span and area are plotted. For a study of interseismic strain accumulation, both a long duration and good spatial coverage are required. These conditions are not met by any subset of the Denali Fault interferograms.

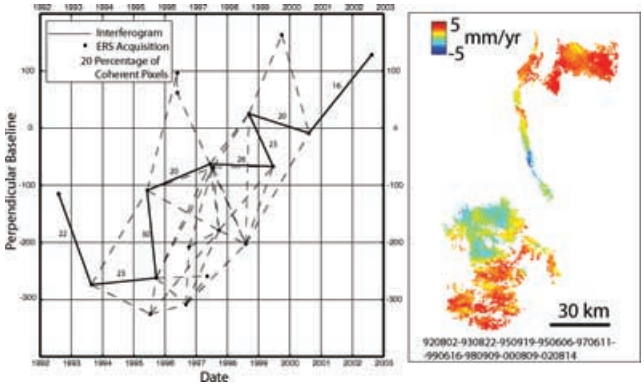

Figure 9. Result of stacking a chain of interferograms covering a total time period of 10 yr. The resulting stack is still dominated by atmospheric and orbital contributions.

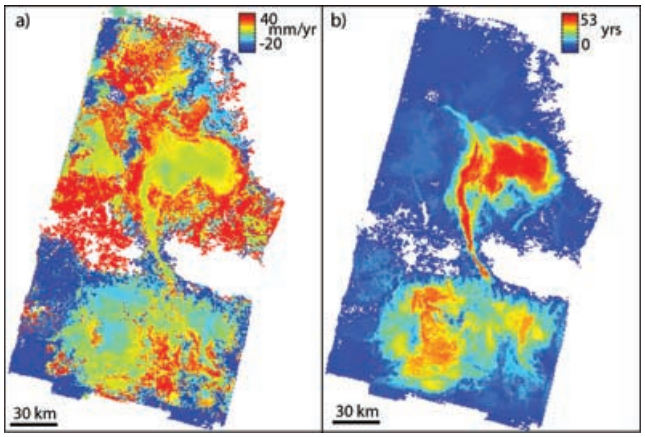

Figure 10. (a) Average deformation rate at each pixel taken from all interferograms that are coherent at that pixel. The interferograms are dominated by orbital rather than tectonic contributions so the resulting rate map contains discontinuities. (b) Cumulative duration of interferograms which are coherent at each pixel.

the chain cancel leaving only the contributions from the first master and last slave.

The chain can be made of short time-period interferograms which do not suffer so much from temporal decorrelation so the coherence will be significantly better than a single interferogram covering the same time-span. The longest chain that can be made from interferograms covering the Denali Fault has a duration of 10 yr which corresponds to a predicted tectonic contribution of 20 mm when projected into the satellite line of sight. However, the resulting stack is still dominated by atmospheric and orbital contributions (Fig. 9).

3.3 Simple rate maps

So far the methods discussed rely on pixels which are coherent throughout the data set but pixels which are only coherent in some of the interferograms still contain useful information about deformation rate. In order to compare pixels which are coherent in different numbers of interferograms, it is necessary to view the data in terms of deformation rate rather than total deformation. The simplest way to do this is to stack all the interferograms and divide by the cumulative duration of the interferograms which are coherent at each pixel (Fig. 10). Alternatively, each interferogram, which measures the total deformation between the dates of the master and slave acquisitions, can be converted into an average deformation rate by dividing by the time span of the interferogram. Assuming interseismic deformation builds up at a constant rate, this should be the same in any interferogram for a given pixel. A mean rate for each pixel can be found by least-squares fitting these rate values using whichever interferograms are coherent at that pixel and weighting the inversion using our previous estimates of noise.

Both methods assume that the values in the interferogram are proportional to the duration of the interferograms. This is true for the tectonic signal but not the orbital or atmospheric components. If adjacent pixels are coherent in a different number of interferograms, our rate estimation methods will divide the adjacent values by different durations resulting in a jump (Fig. 10).

3.4 Time-series methods

Time-series methods (Berardino *et al.* 2002; Schmidt & Burgman 2003; Lanari *et al.* 2004) are typically used to study deformation sources which vary significantly with time, such as aquifer and oil extraction signals. The details of the methods vary but use a linear inversion on data from a large number of interferograms to create a time-series of incremental range change on the date of each acquisition. The permanent scatterers technique (Ferretti *et al.* 2000) focuses on point scatterers which do not suffer geometric decorrelation and so use can be made of a much larger archive of data. This method has proved particularly effective in studying urban areas which have a high density of permanent scatterers (Burgmann *et al.* 2006), and with some modification, can be applied to more remote areas (Hooper *et al.* 2004), however, it has yet to be tested on an area with terrain similar to Alaska.

These methods rely on pixels or points which are coherent in all interferograms so cannot be applied to areas such as Denali.

4 SYNTHETIC INTERFEROGRAMS

We use the analysis presented in Section 2 to create a data set of synthetic interferograms in order to test a variety of techniques against known values and understand the effect of each of the various phase contributions.

Our approach is based on the assumption that the phase in each interferogram, ϕ_{mn}, is composed of five components: the deformation signal, orbital contribution, atmospheric contribution, offset from the reference pixel and an error term, ϵ which includes contributions from thermal noise, interpolation errors, filtering etc.

$$\phi_{mn} = \frac{4\pi}{\lambda}(t_m - t_n)r_{los} + (\phi_{orb,m} - \phi_{orb,n}) + (\phi_{atm,m} - \phi_{atm,n}) + w_{mn} + \epsilon. \quad (2)$$

The phase contribution from ground deformation is proportional to the interferogram duration $(t_m - t_n)$. The rate of displacement in the satellite line of sight (los), $r_{\rm los}$, is taken from the deep-fault model presented in section 1.1. Both the orbital, $(\phi_{{\rm orb},m} - \phi_{{\rm orb},n})$ and atmospheric contributions, $(\phi_{{\rm atm},m} - \phi_{{\rm atm},n})$, can be seen as linear combinations of the errors in the complex radar images used to produce the interferogram. The offset to the reference pixel, w_{mn}, is constant for each interferogram and is a random number which depends on which seed location is chosen for unwrapping.

In order to approximate a suitable orbital contribution for each acquisition, we find the mean and standard deviation of the orbital

© 2007 The Authors, *GJI*, **170,** 1165–1179
Journal compilation © 2007 RAS

parameters estimated in Section 2.3 and use them to produce a set of random orbital parameters with the same statistical properties. We assume the orbital errors are uncorrelated, $\sigma_{mn}^2 = \sigma_m^2 + \sigma_n^2$, where σ_{mn} is the error on the interferogram and σ_m is the error on the acquisition. Since the orbital errors are of similar magnitude throughout the data set, we can assume that $\sigma_m \sim \sigma_n$, implying that the orbital parameters for each acquisition will be smaller than that for the interferogram by a factor of $\sqrt{2}$. Applying this scaling factor to the set of orbital parameters randomly generated for the interferograms results in a set of orbital parameters for each acquisition which can then be used to produce an appropriate orbital contribution for each pixel of each acquisition.

Similarly the atmospheric parameters for each interferogram found in Section 2.3 are converted into an atmospheric phase screen for each acquisition by creating a synthetic atmospheric phase screen for an interferogram and dividing by a factor of $\sqrt{2}$ to convert to an atmospheric phase screen for an acquisition.

We create atmospheric phase screens for a set of interferograms using the parameterisation of atmospheric noise discussed in Section 2.4. The decay distance and variance are assumed to be constant and the value chosen are the median values, $\bar{\alpha} = 12.3$ km and $\bar{\sigma} = 7.5$ mm. These are then converted into correlation coefficients which can be used to create a variance–covariance matrix for a sparse grid of datapoints. A Cholesky factorisation is used to produce values at each datapoint with the correct statistical properties (Parsons *et al.* 2006). The sparse grid is then interpolated to the required resolution.

We combine the tectonic contribution for the appropriate duration with orbital and atmospheric contributions to produce interferograms with the same distribution of master and slave images as for the Denali test data set. We use the coherence masks for a threshold of $\gamma = 0.15$ derived from the actual Denali interferograms to simulate the effects of temporal and geometric decorrelation (see Fig. S3 in the Supplementary Material).

5 ITERATIVE SLIP RATE ESTIMATION WITH NETWORK ORBITAL CORRECTION

5.1 Algorithm overview

In order to measure fault slip rate, we use an iterative algorithm with three steps; orbital error correction, construction of a rate map, and estimation of the fault slip rate (Fig. 11). The first step estimates and removes the orbital error on each acquisition. Next, we estimate the best-fitting deformation rate at each pixel based on whichever interferograms are coherent and produce a rate map and associated error map. The last step is to invert the rate map to find the best fitting slip rate using assumptions about the geometry of the fault.

On the first pass, the slip rate is underestimated due to the long-wavelength similarities between orbital error and interseismic strain. To adjust for this, we iterate the procedure by removing from the interferograms a model produced using the best-fitting slip rate, re-estimating the orbital error and adding back in the model. An *a priori* estimate of slip rate from alternative data could be used to be reduce the number of iterations required. We illustrate the method using synthetic data constructed using the techniques described in Section 4. We test our algorithm on two examples; the first is purely the tectonic component, with a slip rate of 40 mm yr^{-1} and secondly using the same tectonic component but with additional atmospheric and orbital contributions. We average the pixel values in the original

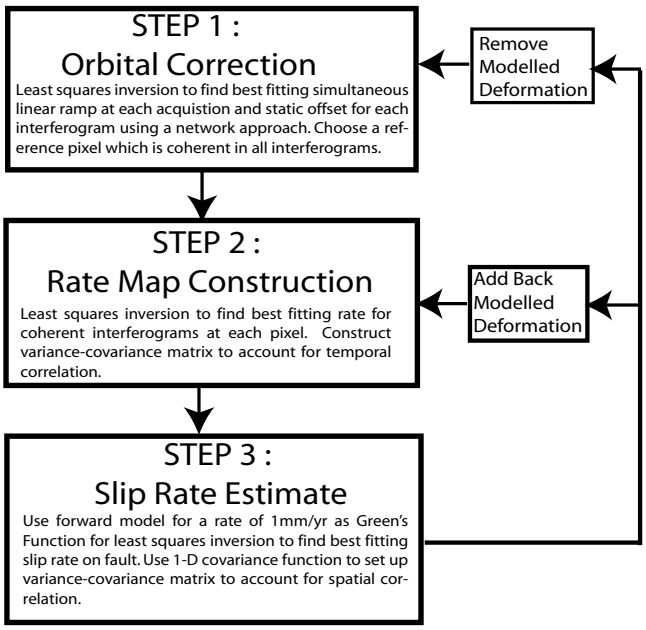

Figure 11. Flow chart showing the algorithm for analysing interseismic strain accumulation using distributed scatterer interferograms in areas where coherence is variable.

interferograms to produce a pixel size of 6.4 km, in part, to reduce the number of datapoints within the data set for ease and speed of calculation, but also to reduce the correlation of the atmospheric contribution between adjacent pixels.

Testing on synthetic data allows us to verify that the algorithm accurately reproduces the input parameters, identify any trade-offs or systematic bias, and find the range of slip rates for which the algorithm is applicable.

5.2 Network orbital correction

Most previous studies estimate the orbital contribution on interferograms individually. However, each acquisition is used to construct several interferograms and so it is possible to estimate the orbital contribution to a single acquisition using constraints from many interferograms. Therefore, we prefer to use a network approach to empirically estimate the orbital error on each acquisition rather than each interferogram.

We have already demonstrated in Section 2.5 that the orbital contributions to interferograms behave in a conservative manner and can be thought of as the difference between the orbital contributions to each acquisition. Initially we assume the interferogram is dominated by the orbital contribution and any other contribution is considered a source of noise. Assuming a planar orbital error, for a pixel, p, at location $[x_p, y_p]$, the phase in the interferogram, ϕ_{lm} can then be written as a linear function of two parameters, u and v, for each of the acquisitions, m and n, and a reference frame shift for the interferogram, w_{mn}

$$\phi_{mnp} = u_m x_p - u_n x_p + v_m y_p - v_n y_p + w_{mn}. \quad (3)$$

Similar equations can be written for each coherent pixel in each interferogram.

This approach separates the long wavelength component (due to orbital errors and long wavelength ionospheric and tropospheric delays), which behaves as a linear combination of the long wavelength components on the acquisitions, from the long wavelength tectonic

signal, which is simply related to the duration of the interferogram. Short duration interferograms, which are often ignored because they have only a small component of deformation, provide valuable additional constraints to improve the estimates of the orbital component. The value w_{mn} is a reference frame shift which takes into account the different seed locations used when unwrapping each interferogram.

Problems of this kind are intrinsically underdetermined since there will always be at least one fewer interferogram than the number of acquisitions. For a system of N interferograms with P pixels constructed using A acquisitions, there are $2A + N$ unknowns and NP observations, however, not all these observations act as independent constraints, the rows of the design matrix are linearly related giving a rank of $2(A - 1) + N$. We use a truncated singular value decomposition to find the minimum norm solution using a threshold of 2×10^{-9} for truncating the singular values. This approach distributes the remaining orbital error, which cannot be solved for, across the existing orbital corrections, leaving an additional planar tilt and offset which must be corrected for at a later stage in the algorithm. For 90 m resolution, each interferogram contains roughly one million pixels making a total of 4.4×10^7 observations. However, since we are primarily interested in long wavelength features, this stage can be carried out at a much lower resolution, for example a pixel size of 6.4 km reduces the number of observations to a more manageable 7500. The variance–covariance matrix for these observations would contain 55 million elements. Although the matrix would be sparse, we make the assumption that the observations are uncorrelated and equally noisy and perform the inversion without a variance–covariance matrix.

Once the orbital parameters have been estimated, they can be used to construct a full resolution version of the orbital contribution for each interferogram and then removed (Fig. 12).

A comparison between the estimation of orbital errors using the network approach versus the simple planar approximation used in Section 2.3 is shown in Fig. 13. The test is carried out on a set of synthetic interferograms composed of a planar orbital error, atmospheric and interseismic deformation contributions. The network orbital correction technique reduces the rms misfit between input parameters and correction parameters from 0.118 to 0.107 mm km^{-1} in the x-direction and from 0.194 to 0.180 mm km^{-1} in the y-direction; an improvement of 5–10 per cent. The accuracy of the ramp parameters for an individual interferogram depends on the coherent area available, so for interferograms with poor coherence, the errors on the estimated ramp parameters are large. By using the network approach we improve the estimates for these interferograms, by using information from interferograms for which the orbital parameters are best constrained. Hence we are able to produce an overall improvement in the orbital correction despite reducing the number of free parameters.

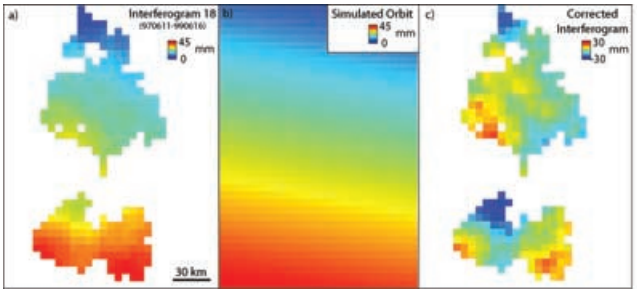

Figure 12. Results of network approach to orbital correction. (a) Interferogram number 18 (970611–990616). The interferogram is dominated by a long-wavelength orbital component. (b) Simulated orbit using network correction. (c) Interferogram after network orbital correction. The long-wavelength orbital component has been removed, and the dominant component is now atmospheric. Note change in colour scale. The pixel size is 6.4 km to reduce calculation time.

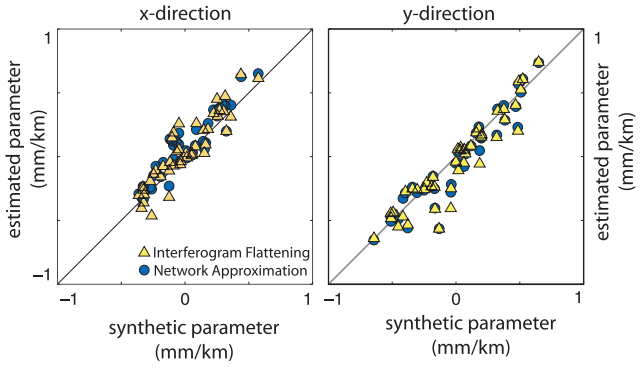

Figure 13. Comparison between methods of estimating orbital parameters from synthetic interferograms composed of a planar orbital error with contributions due to the atmosphere and interseismic deformation. The network approximation (blue circles) reduces the root mean square misfit from 0.118 to 0.107 mm km^{-1} in the x-direction and 0.194 to 0.180 mm km^{-1} in the y-direction when compared to the traditional method based on individual interferograms (yellow triangles).

5.3 Rate map formation

It is necessary to combine measurements from pixels which are coherent in some but not all the interferograms. We use a least-squares matrix inversion on a pixel-by-pixel basis to find the best fitting rate, $r_{\rm los}$, from the available interferograms at each pixel (Fig. 14a).

$$\frac{2\pi}{\lambda}\mathbf{T}r_{\rm los} = \mathbf{P}, \tag{4}$$

where $\mathbf{T}$ is a vector containing the time-spans, $[t_{12}, t_{23}, t_{34} \ldots t_{mn}]^T$, and $\mathbf{P}$ is a vector containing the phase, $[\phi_{12}, \phi_{23}, \phi_{34} \ldots \phi_{mn}]^T$ for each interferogram which is coherent at that pixel.

The inversion is weighted using a variance–covariance matrix, $\Sigma_{\rm P}$, to take into account the atmospheric and orbital noise at each interferogram and the correlation between interferograms. The element σ_{lm-nq} of the variance–covariance matrix, $\Sigma_{\rm P}$ corresponding to the interaction between interferograms lm and nq depends on the atmospheric error estimate for each interferogram σ_{lm} and σ_{nq}, the orbital error estimate on each pixel, σ_p, and the correlation between

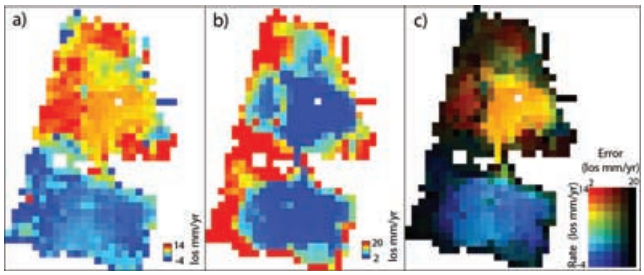

Figure 14. Rate and error maps for synthetic data using a slip rate of 40 mm yr^{-1} with atmospheric and orbital contributions. (a) Rate map. Pixels to the north of the fault have higher line-of-sight rates (red), with lower rates (blue) south of the fault reflecting right lateral tectonic deformation. (b) Error map. The errors are lowest at pixels which are coherent in a large number of interferograms. (c) Rate map with intensity inversely proportional to error estimate. Bright pixels are those with the smallest error.

© 2007 The Authors, *GJI*, **170,** 1165–1179
Journal compilation © 2007 RAS

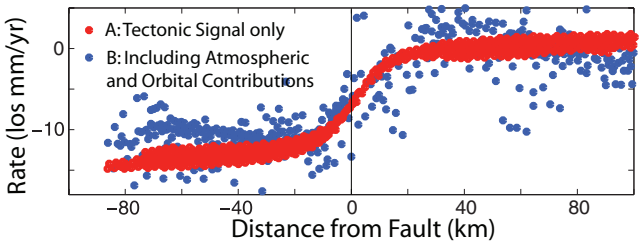

Figure 15. Profiles across the rate maps for synthetic experiments. Each pixel is plotted according to distance from the fault. A (red dots) are taken from synthetic data with only a tectonic component. The scatter of the pixels around an inverse tangent function is caused by changes in the line-of-sight vector across the track. B (blue dots) are from synthetic data with tectonic, atmospheric and orbital contributions. The additional orbital and atmospheric contributions further increase the scatter and introduce a long-wavelength tilt which is removed by iteration.

interferograms.

$$\sigma_{lm-nq} = \left(\sigma_{lm}\sigma_{nq} + \sigma_p^2\right)c_{lm-nq}. \tag{5}$$

If the interferograms, lm and nq, have a common master or a common slave ($l = n$ or $m = q$), $c_{lm-nq} = 0.5$; if the master of one interferogram is the slave of the other ($l = q$ or $m = n$), $c_{lm-nq} = -0.5$ and at $l = n$ and $m = q$, $c_{lm-nq} = 1$. For the sake of simplicity, the atmospheric error, σ_{lm}, on each interferogram is assumed to be constant and the value chosen is the median value of 7.5 mm from the analysis of atmospheric noise in Section 2. Since a common reference pixel is used for all the interferograms, errors in the orbital adjustment increase with distance from this point. The orbital error parameter for each pixel, σ_p, is based on its distance from the reference pixel and an assumed slope of 2.6 mm per pixel in the x-direction (0.41 mm km^{-1}) and 1.7 mm per pixel in the y-direction (0.27 mm km^{-1}) given by the standard deviation values of gradients calculated in Section 2.3. Since the inversion is carried out on a pixel by pixel basis, it is not necessary to include the spatial correlation between pixels. The rate and associated error at each pixel (Fig. 14b) is given by,

$$\mathbf{r}_{\text{los}} = \frac{\lambda}{2\pi}[\mathbf{T}^T\Sigma_{\mathbf{P}}{}^{-1}\mathbf{T}]^{-1}\mathbf{T}^T\Sigma_{\mathbf{P}}{}^{-1}\mathbf{P} \tag{6}$$

$$\Sigma_{\mathbf{r}} = [\mathbf{T}^T\Sigma_{\mathbf{P}}{}^{-1}\mathbf{T}]^{-1}. \tag{7}$$

For the synthetic tests, the rate of strain accumulation is sufficiently rapid that the interseismic signal clearly dominates the pixel values in the rate maps (Fig. 14). The reliability of the values at each pixel depends on the number and distribution of interferograms which are coherent at that pixel so we use the values from the error map to determine the intensity of the pixels such that bright pixels have low *a priori* errors (Fig. 14c). We create swath profiles across the rate maps by plotting each pixel value against perpendicular distance from the fault. In the case of the noise-free test, the profile takes the form of an inverse tangent as expected (Fig. 15) with spread caused by variations in the satellite line-of-sight between pixels. A similar profile from the test including noise shows additional scatter caused by the atmospheric errors, but still follows the prediction for a slip rate of 40 mm yr^{-1}.

5.4 Slip rate estimate

We wish to estimate the slip rate on the fault, s, from the rate and error maps we have produced. For an assumed fault geometry and

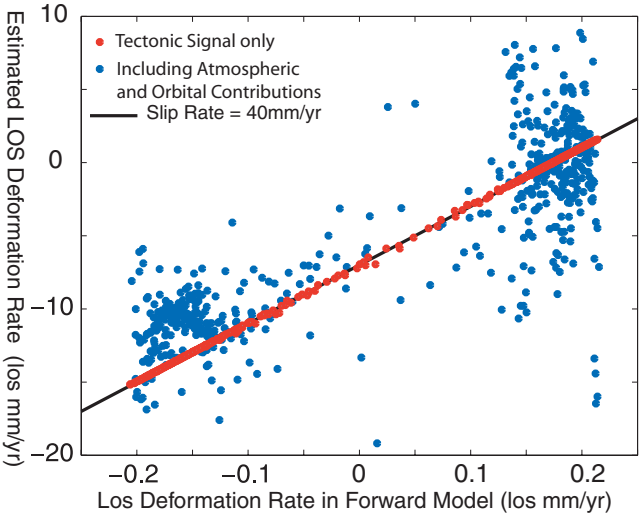

Figure 16. Correlation between pixel values in a forward model of tectonic deformation (horizontal axis) and the rate map. For A (red dots) where the only component in the interferograms is tectonic, the correlation is perfect and the point fall on a straightline. The gradient of the line reflects the slip rate on the fault. For B (blue dots), the orbital and atmospheric contributions increase the scatter around the line, but do not alter the gradient.

locking depth, we model the rate of ground deformation expected for a nominal slip rate (1 mm yr^{-1}). We use a simple deep fault model (Section 2.2). We expect the ground deformation to scale linearly with slip rate so a direct comparison of the corresponding pixel values in the rate map and the forward model should result in a straight line. The noise free test shows perfect correlation between the forward model and rate map, with the slope of the line reflecting the slip rate. For the test including noise, the points no longer fit on a perfect straight line, but the correlation is clear (Fig. 16).

Similarly, the forward model can be used as a Green's function for a linear least-squares inversion to find the slip rate, s,

$$r_p = sf_p + gx_p + hy_p + q, \tag{8}$$

where r_p are pixel values from the rate map and f_p are the corresponding pixel values from the forward model. The additional parameters g, h and q are included to allow for the planar tilt and offset between the forward model and rate map which resulted from in using the minimum norm solution to the network orbital correction. The inversion is weighted using a variance–covariance matrix, Σ_P which takes into account the error estimates on each pixel and the spatial correlation between pixels. The elements, σ_{jk}, of the variance–covariance matrix, Σ_P, are constructed using $\sigma_{jk} = \sigma_j\sigma_k c_{jk}$, where σ_j are the error estimates on each pixel producing during formation of the rate map and c_{jk} is the spatial correlation between the pair of pixels. We estimate the correlation coefficients, c_{jk} using the exponential form with average value $\bar{\alpha} = 12.3$ km from the analysis of the Denali data set (Section 2.4).

For the synthetic test using only the tectonic signal, the initial slip rate estimate is 38 mm yr^{-1}. This is because some of the long-wavelength interseismic signal 'leaks' into the orbital adjustment, (which should be zero in this test); the orbital errors are overcorrected. For further iterations, an approximate slip model is removed before the orbital estimation step so that, although a similar proportion of the remaining interseismic signal is mistakenly identified as orbital error each time, as the slip model improves, so does the orbital error estimate. The absolute error is reduced with each iteration, gradually converging on the correct value. The algorithm

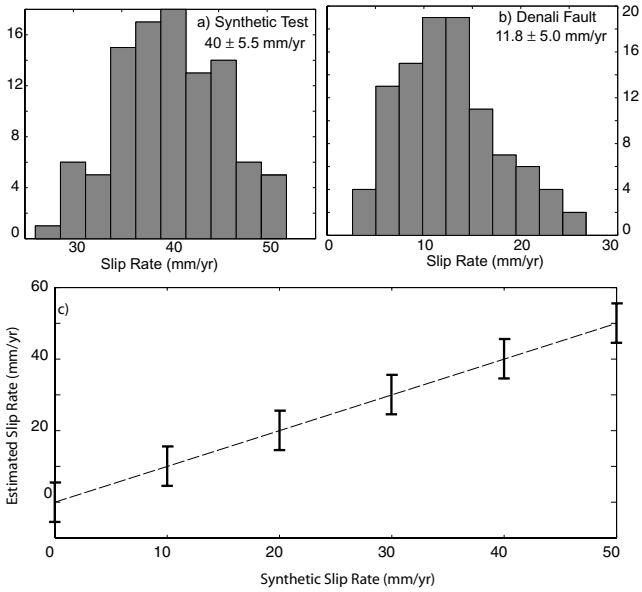

Figure 17. Monte Carlo error estimates on slip rate for (a) synthetic data with a slip rate of 40 mm yr^{-1} (b) interferograms from the Denali Fault to which synthetic noise has been added. Slip rate is found for 100 sets of synthetic data with suitable atmospheric and orbital characteristics. (c) Results of synthetic tests on a range of slip rate. Error bars are the result of Monte Carlo error analysis and are independent of slip rate.

converges logarithmically on a value of 40.0399 (4d.p.) which is accurate to better than 0.1 mm yr^{-1}. The number of iterations necessary depends on the accuracy required.

For the synthetic which included noise, the best fitting slip rate is again 40.0 mm yr^{-1}. Since we use variance–covariance matrices to weight our inversions at each stage of the algorithm, we produce an *a priori* estimate of the error on the slip rate. This significantly underestimates the scatter in results, probably because the spatial correlation between pixels is underestimated, so we prefer to use a Monte Carlo method for a more realistic error estimate. The Monte Carlo method involves creating 100 perturbed data sets using simulated noise. Noise is simulated in the same way as described in Section 4. The results of a Monte Carlo error analysis for test B shows an average slip rate of 40.1 mm yr^{-1} with a one sigma error of 5.5 mm yr^{-1} (Fig. 17). Synthetic tests using a range of slip rates between 0 and 50 mm yr^{-1} for interferograms containing orbital and atmospheric contributions show that the Monte Carlo error varies little with slip rate (Fig. 17c).

Tests using forward models with different locking depths show that there is considerable trade-off between locking depth and slip rate, with greater locking depths requiring higher slip rates to match the same surface observations. The locking depth is poorly constrained by the data so use must be made of *a priori* estimates of the thickness of the seismogenic zone. For example, for synthetic data constructed using a locking depth of 10 km and slip rate of 40 mm yr^{-1}, slip rate estimates range from 28 ± 3 mm yr^{-1} for an assumed locking depth of 2 km to 51 ± 8 mm yr^{-1} for an assumed locking depth of 20 km.

6 DENALI FAULT

We now apply this algorithm to the Denali Fault in Alaska and compare our estimates of slip rate to those from other methods, both geodetic and geological. The interferograms are taken from our test

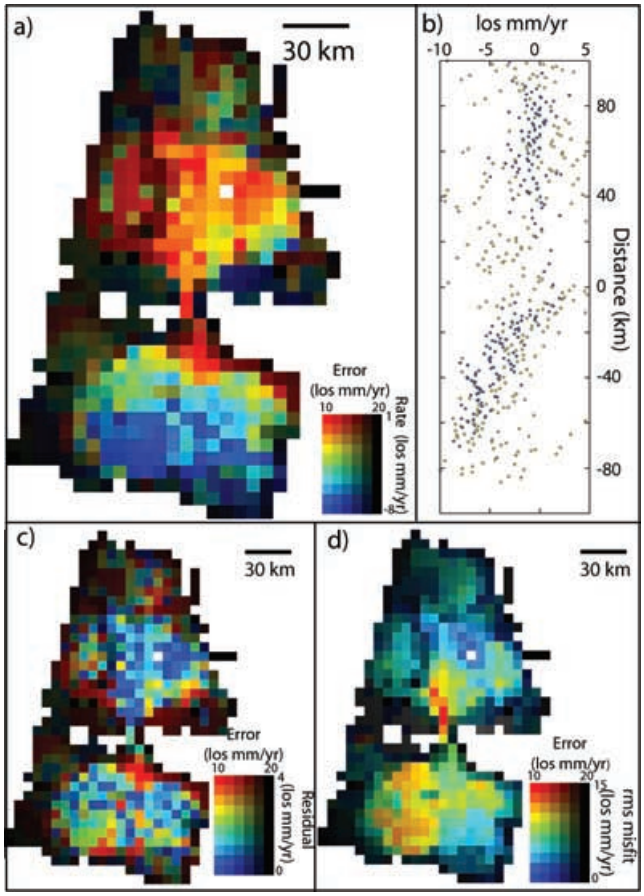

Figure 18. Denali Fault: (a) rate map after three iterations; (b) profile across the rate map. Filled dots represent pixels whose error estimate is less than 3 mm yr^{-1}; (c) residual between rate map and model and (d) rms of residuals between individual interferograms and model interferograms created from rate map and orbital corrections.

track (329), which is described in Section 2. In order to apply this algorithm directly, we assume the fault is purely strike-slip with no vertical motions and ignore other sources of surface deformation. In both cases, these assumptions are oversimplifications since the presence of the Alaska Range indicates uplift and GPS data show deformation from subduction zone extends this far inland. Deformation associated with the flow of glaciers is removed from the interferograms before the algorithm is applied.

The best-fitting slip rate found using our algorithm is 10.5 mm yr^{-1}. The rate map shows a clear step at the location of the Denali fault with positive deformation rates (towards the satellite) to the north and negative deformation rates to the south (Fig. 18a). The Monte Carlo error estimate on the slip rate is ±5.0 mm yr^{-1} (Fig. 17b).

We construct maps of the residual between the interferograms, rate map and model to identify any additional components in the interferograms which we have not accounted for. In order to study the residual between the rate map and the tectonic model, a model rate map is produced by scaling the forward model by the slip rate estimate. Systematic patterns in this residual may indicate non-random errors caused by contributions to ground deformation not accounted for by the simple tectonic model. The residual left when a model rate map is removed from the actual rate map has a median value of 2.3 mm yr^{-1} (Fig. 18c). The only exception is in the region close to the fault, where the misfit is up to 5 mm yr^{-1} which could be

© 2007 The Authors, *GJI*, **170,** 1165–1179
Journal compilation © 2007 RAS

attributed to a range of causes such as an inaccurate locking depth, complex geometry or multiple fault strands.

In order to assess errors in the construction of the rate map, we create synthetic interferograms with orbital contributions based on model parameters produced by our algorithm. The tectonic contribution can be approximated by scaling the rate map according to the duration of the interferogram. The residual between the synthetic interferograms and the original interferograms should be equivalent to the atmospheric contribution. Fig. 18(d) shows the rms value of the residual for each pixel. For all interferograms, the residual at the reference pixel is zero. The residual grows radially outwards from the reference point reaching a maximum of about 15 mm. Overall, the rms value of the rms residuals is 6.1 mm comparable to our estimate for atmospheric noise in this region.

As with the synthetic data, there is significant trade-off between slip rate and locking depth for the Denali Fault data (Fig. 19a). *A priori* estimates of the thickness of the seismogenic layer vary, with the peak coseismic slip occurring to depths of 9 km (Hreinsdottir *et al.* 2006) and aftershocks occurring to depths of 11 km (Ratchkovski *et al.* 2004).

7 DISCUSSION

We have presented a new method for finding the interseismic slip rate on a fault under difficult interferometric conditions. A number of possible improvements to the algorithm suggest themselves, mostly related to the oversimplification of the functional model for interseismic strain accumulation. It is worth noting that although this method was designed with the intention of studying interseismic strain accumulation, it could be applied to any source of ground deformation for which the geometry is known. Here we discuss plans for future modifications to the algorithm and compare our preliminary result for slip rate on the Denali Fault to other estimates.

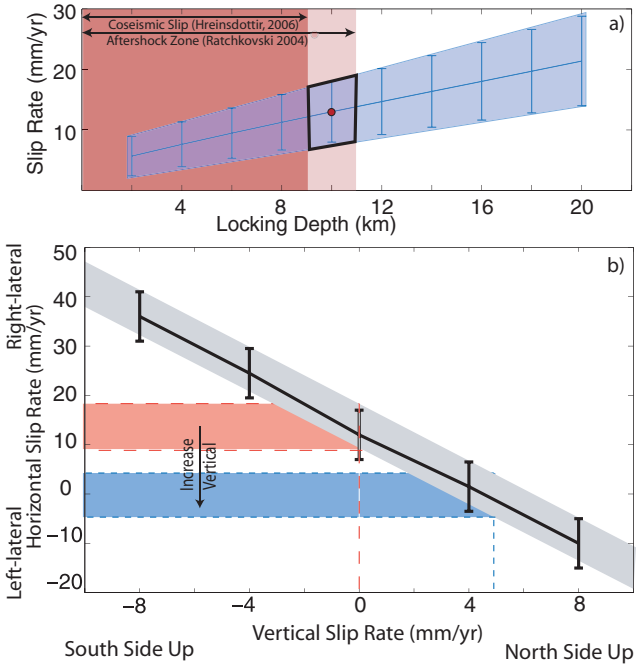

Figure 19. Trade-off between locking depth and slip rate for estimates of interseismic strain accumulation on the Denali Fault.

7.1 Future improvements to the algorithm

The network orbital correction technique offers a significant improvement (5–10 per cent) over traditionally methods applied to individual interferograms. However, the orbital errors are more complex than the planar approximation used here. Even assuming a flat earth geometry, the cross-track error will vary with look angle rather than linearly. Ideally, we would estimate the orbital parameters such as parallel and perpendicular baseline directly using a spherical geometry.

Our model assumes that all motion is horizontal and parallel to the fault. The presence of the Alaska Range, including the 6000 m peak of Mt McKinley, indicates that some vertical motion, albeit possibly distributed, is occurring. A significant vertical component of motion was observed during the 2002 earthquake (Hreinsdottir *et al.* 2006). Apatite fission track data from the Denali Region indicates a mean surface uplift of 0.5 mm yr^{-1} since the onset of rock uplift at 5–6 Ma (Fitzgerald *et al.* 1995). The vertical motions, although likely to be smaller than the horizontal motions, are important because the incidence angle of 23° of the ERS satellites means they dominate the measurements taken in the line of sight. Our algorithm could easily be modified to allow for variable rake by solving for two slip rate parameters, one horizontal and one vertical. Furthermore, the inclusion of data from both ascending and descending passes of the satellite rather than a single test track would allow us to distinguish between horizontal and vertical motions.

The geometry of our model is oversimplified, a single linear fault model is appropriate for our synthetic data, but the Denali Fault itself has significant curvature in this region. We are also considering the Denali Fault in isolation, ignoring other sources of ground deformation in the region. Possible tectonic influences include the effects of plate coupling at the subduction zone which may add a potential bias to the south of Denali fault. The SAR look angle is particularly sensitive to vertical motions. While it is possible to build vertical motions along the Denali Fault into more complex models of fault geometry, non-tectonic vertical motions, such glacial isostatic adjustments (GIA) may add a potential bias to the system. The southeast of Alaska is known to be uplifting rapidly in response to glacial melting following the Little Ice Age (Larsen *et al.* 2005). However, both the subduction zone and GIA signals are far-field effects and sufficiently long-wavelength for our algorithm to incorporate them into the network orbital correction rather than the model of fault slip.

Recent analysis of vertical GPS measurements (J. Freymueller *et al.*, personal communication) suggest there may be a significant vertical step of as much as 5–6 mm yr^{-1} across the Denali Fault (north side up). To test the effects of this on our InSAR analysis, we impose a range of vertical slip rates on our deep fault model and solve for the remaining horizontal slip rate (Fig. 19b). The signal in the InSAR data can be matched by a vertical slip rate of 1.9 ± 1.5 mm yr^{-1} alone, without requiring any horizontal motion. The steep incidence angle of ERS/Envisat (23°) means that only a small vertical displacement is required to account for the observed change in line-of-sight. Whilst the notion of vertical motion on a vertical, deep fault is not considered physically realistic, it serves as a rough approximation for the type of step observed in the GPS data. The trade-off between horizontal and vertical motions will be significantly reduced when considering multiple InSAR tracks from different look directions and so this issue is left as a subject for future study. The assumption of purely horizontal motion on major strike-slip faults is common place in other interseismic studies (e.g. Peltzer *et al.* 2001; Wright *et al.* 2001, 2004a; Fialko 2006) and even small amounts

of vertical motion may have significant implications for slip rate estimates.

The deep-fault model can be considered unrealistic for both theoretical and observational reasons. As temperature increases with depth, the dominant deformation mechanism of quartz changes from brittle failure to dislocation creep. As a result, deformation is no longer localized on discrete planes but is distributed throughout the medium. As a result, a shear zone model of deformation below the seismogenic layer may be more realistic than a simple deep-fault model (Prescott & Nur 1981; Bourne *et al.* 1998). Attempts to model observations of post-seismic deformation mostly use layered structures with complex rheology (e.g. Pollitz *et al.* 2000). GPS data from the first 2 yr following the 2002 Denali Fault earthquake have been modelled using a combination of flow within a viscoelastic mantle extending from 60 km down, lower crustal flow (or afterslip) at depths of 15–60 km and poroelastic rebound (Freed *et al.* 2006). A truly satisfactory model of rheological structure should be consistent with all phases of the earthquake cycle. However, because deformation at the surface is filtered through an elastic lid, features with a half-wavelength narrower than πL, where L is the thickness of the elastic lid cannot be resolved (Savage 1990). Thus, for a seismogenic thickness of 15 km, a shear zone narrower than 50 km could not be distinguished from the single fault implied by the deep fault model from surface observations. Integrating geodetic observations of the present-day deformation field with longer term geological constraints on factors such as slip rate and earthquake recurrence intervals it may be possible to produce models which are more compatible with our physical expectations of fault-structure at depth (Segall 2002).

The Denali Fault is a crustal scale suture, marking the geological boundary between the Yukon-Tanana terrane to the north and the Wrangellia composite terrane to the south. The elastic shear modulus, as inferred from seismic velocities, shows a clear discontinuity coincident with the trace of the Denali Fault at depths ranging from 33 to 65 km (Eberhart-Phillips *et al.* 2003; Freed *et al.* 2006). This suggests that the shear zone at depth is narrow and a deep-fault model, whilst not necessarily geologically accurate, is a justifiable simplification in this case. The width of the shear zone beneath the seismogenic layer has little impact on far-field surface observations so to use InSAR studies to provide more constraints on this aspect of interseismic deformation would require higher resolution or a more distance based subsampling algorithm to improve the near-field resolution.

Another possible complication would be the presence of shallow creep (Wesson 1988). Shallow creep has been observed on several major strike-slip faults including the North Anatolian Fault and several strands of the San Andreas Fault System. No such creeping segment has been identified on the Denali Fault, but since creep is most often identified through the offset of man-made structures, in the remote areas of Alaska through which the Denali Fault passes it is possible that a creeping section of fault might remain unnoticed. Creep near the surface would be easily observable as a sharp offset in the interferograms (e.g. Burgmann *et al.* 1998), something which we have not seen.

The errors associated with this technique of 5–6 mm yr^{-1} make it suitable for measuring faults with rapid slip rates. However, in order to study a wider range of faults including those with lower slip rates, for example, less than 5 mm yr^{-1}, the errors need to be further reduced. The dominant remaining source of error is atmospheric water vapour. Ongoing attempts are being made to model and remove the atmospheric contribution using GPS data (Li *et al.* 2005), satellite water vapour measurements from instruments such as MODIS and MERIS, (Li *et al.* 2006, 2005) and atmospheric models (Wadge *et al.* 2002; Foster *et al.* 2006). However, the most effective method at this stage is still the brute force approach of increasing the size of the data set. The Denali Fault is at sufficiently high latitude that the ground tracks overlap; six tracks cover the Delta River Valley. In the future, newer satellites such as Radarsat and Envisat may produce a higher density of acquisitions even at lower latitude by making use of wide-swath and variable beam mode capabilities. A separate rate map would need to be constructed for each track of data, but these could then be combined into a single slip rate estimate before iteration.

Atmospheric water vapour is often correlated with topography, since the path length through the atmosphere will be reduced over high mountains. Unfortunately, many major tectonic features correspond to major topographic features, including the Denali Fault which cuts through the Alaska Range. As a result it may be difficult to separate the atmospheric contribution associated with topography from the tectonic signal. A possible solution would be to use our network approach and including a term for each acquisition which is proportional to topography.

7.2 Comparison to previous slip rate estimates

Our estimate of interseismic slip rate on the Denali Fault of 10.5 $\pm$ 5.0 mm yr^{-1} is, to within error, compatible with previous estimates from both geodetic (GPS) and geological sources giving confidence that the method presented here works well for slip rates as low as 10 mm yr^{-1} and in areas of poor coherence. The InSAR result is slightly higher than previous geodetic estimates based on GPS measurements and is much closer to the geological estimate of 12.0 $\pm$ 1.7 mm yr^{-1} (Matmon *et al.* 2006). However, given the error bars involved when using a single track of data, this comparison may not be significant. By combining numerous tracks of data from both ascending and descending passes, it should be possible to reduce the error on the InSAR result down to 1–2 mm yr^{-1} allowing for a more robust comparison.

In central Alaska the Denali Fault has often been approximated by a small circle and is sometimes modelled as a rotating block (Fletcher 2002; Freed *et al.* 2006). In this case, the slip rate along the length of the Denali Fault would be expected to be constant. However, this approach assumes that the Denali Fault is the only active structure in the region. The study of Matmon *et al.* (2006) suggests that the curvature of the Denali fault is responsible for a westward decrease in slip rate and increase in shortening. Observations of seismicity during the period 1912–2002 show little activity on the Denali Fault with the majority of significant earthquakes occurring to the north or south of the Denali Fault with thrust mechanisms. In particular, the Northern Foothills is a 40-km wide zone of thrust faulting located between the Parks Highway and Richardson Highway. In this case, structures such as these could accommodate a proportion of the tectonic stress and variations in slip rate along the fault would be expected.

8 CONCLUSIONS

InSAR has the potential to produce continental-scale maps of fault slip rate but our ability to measure slow, long wavelength deformation signals is currently limited by decorrelation (both temporal and spatial), orbital errors and atmospheric errors. In order to reduce the impact of these factors on our measurements, we propose a new algorithm consisting of three stages: orbital error estimation, construction of a rate map and estimation of the slip rate. Using tests

on synthetic data, we find that despite significant levels of noise, the method is capable of not only detecting interseismic signals, but of accurately recovering the slip rate. We apply the method to a single test track of data across the Denali Fault and find a slip rate of 10.5 ± 5.0 mm yr^{-1}; within the range of geological estimates, but slightly larger than found using GPS (Fletcher 2002). It is worth noting that this is just a preliminary result and analysis of data from overlapping tracks on both ascending and descending paths and from other satellites (e.g. Radarsat, JERS) should reduce the errors. Furthermore, using data from multiple look directions should allow us to distinguish between purely strike-slip motion and any vertical component.

ACKNOWLEDGMENTS

This work was supported by the Natural Environmental Research Council (NERC) through the Centre for the Observation and Modelling of Earthquakes and Tectonics. We thank Roland Burgmann, Jeff Freymueller and one anonymous reviewer for their comments. ERS-1/ERS-2 images are copyright 1992–2002 European Space Agency and were provided by the ASF. We thank ASF staff members for their special effort in delivering the imagery on a timely basis.

REFERENCES

Anderson, G. & Ji, C., 2003. Static stress transfer during the 2002 Nenana Mountain-Denali Fault, Alaska, earthquake sequence, *Geophys. Res. Lett.,* **30,** doi:10.1029/2002GL016724.

Berardino, P., Fornaro, G., Lanari, R. & Sansosti, E., 2002. A new algorithm for surface deformation monitoring based on small baseline differential SAR interferograms, *IEEE Trans. Geosci. Remote Sens.,* **40,** 2375–2383.

Bourne, S., England, P. & Parsons, B., 1998. The motion of crustal blocks driven by flow of the lower lithosphere and implications for slip rates of continental strike-slip faults, *Nature,* **391,** 655–659.

Burgmann, R., Fielding, E. & Sukhatme, J., 1998. Slip along the Hayward fault, California, estimated from space-based SAR inteferometry, *Geology,* **26,** 559–562.

Burgmann, R., Hilley, G., Ferretti, A. & Novali, F., 2006. Resolving vertical tectonics in the San Francisco Bay area from Permanent Scatterer InSAR and GPS analysis, *Geology,* **34**(3), 221–224.

Carver, G., Plafker, G., Metz, M., Cluff, L., Slemmons, B., Johnson, E., Roddick, J. & Sorensen, S., 2004. Surface Rupture on the Denali Fault Interpreted from Tree Damage during the 1912 Delta River Mw 7.2–7.4 Earthquake: implications for the 2002 Denali Fault Earthquake Slip Distribution, *Bull. seism. Soc. Am.,* **94,** S58–S71.

Chen, C. & Zebker, H., 2000. Network approaches to two-dimensional phase unwrapping: intractability and two new algorithms, *J. Opt. Soc. Am.,* **17,** 401–414.

Doser, D., 2004. Seismicity of the Denali-Totshunda Fault Zone in Central Alaska (1912–1988) and its relation to the 2002 Denali Fault Earthquake sequence, *Bull. seism. Soc. Am.,* **94,** S132–S144.

Eberhart-Phillips, D., Christensen, D., Brocher, T., Dutta, U., Hansen, R. & Ratchkovski, N., 2003. Imaging the transition from Aleutian subduction to Yakutat collision in central Alaska, with local earthquakes and active source data, *EOS, Trans. Am. geophys. Un.,* **84,** Fall Meet. Suppl., Abstract S21C–01.

Ferretti, A., Prati, C. & Rocca, F., 2000. Non-linear subsidence rate estimation using permanent scatterers in differential SAR interferometry., *IEEE Trans. Geosci. Remote Sens.,* **39**(5), 2202–2212.

Fialko, Y., 2006. Interseismic strain accumulation and the earthquake potential on the southern San Andreas fault system, *Nature,* **441,** 968–971.

Fitzgerald, P., Sorkhabi, R., Redfield, T. & Stump, E., 1995. Uplift and denudation of the central Alaska Range: a case study in the use of apatite fission track thermochronology to determine absolute uplift parameters., *J. geophys. Res.,* **100,** 20 175–20 191.

Fletcher, H., 2002. Crustal Deformation in Alaska measured using the Global Positioning System, *PhD thesis*, University of Alaska, Fairbanks.

Foster, J., Brooks, B., Cherubini, T., Shacat, C., Businger, S. & Werner, C., 2006. Mitigating atmospheric noise for InSAR using a high resolution weather model., *Geophys. Res. Lett.,* **33,** L16304.

Freed, A., Burgmann, R., E., C., Freymueller, J. & Hreinsdottir, S., 2006. Implications of deformation following the 2002 Denali, Alaska, earthquake for postseismic relaxation processes and lithospheric rheology, *J. geophys. Res.,* **111,** doi:10.1029/2005JB003894.

Fuis, G. & Wald, L., 2003. Rupture in South-Central Alaska-The Denali Fault Earthquake of 2002, *U.S. Geological Survey,* pp. Fact Sheet 014–03.

Goldstein, R. & Werner, C., 1998. Radar interferogram filtering for geophysical applications., *Geophys. Res. Lett.,* **25**(21), 4035–4038.

Goldstein, R., Zebker, H. & Werner, C., 1988. Satellite radar interferometry: Two dimensional phase unwrapping, *Radio Science,* **23**(4), 713–720.

Hanssen, R.F., 2001. *Radar Interferometry: Data Interpretation and Analysis,* Kluwer Acad., Norwell, MA, USA.

Hickman, R., Craddock, C. & Sherwood, K., 1977. Stuctural Geology of the Nenana River segment of the Denali Fault system, central Alaska Range, *Geol. soc. Am. Bull.,* **88,** 1217–1230.

Hooper, A. & Zebker, H., in press Phase unwrapping in three dimensions with application to InSAR time series, *J. Opt. Soc. Am.*

Hooper, A., Zebker, H., Segall, P. & Kampes, B., 2004. A new method for measuring deformation on volcanoes and other natural terrains using InSAR persistent scatterers, *Geophys. Res. Lett.,* **31,** L23611.

Hreinsdottir, S., Freymueller, J., Fletcher, H. & Larsen, C., 2003. Coseismic slip distribution of the 2002 Mw7.9 Denali fault earthquake, Alaska, determined from GPS measurements, *Geophys. Res. Lett.,* **30**(13), doi:10.1029/2003GL017447.

Hreinsdottir, S., Freymueller, J., Burgmann, R. & Mitchell, J., 2006. Coseismic deformation of the 2002 Denali Fault earthquake: Insights from GPS measurements, *J. geophys. Res.,* **111,** B01401.

Lanari, R., Lundgren, P., Manzo, M. & Casu, F., 2004. Satellite radar intereferometry time series analysis of surface deformation for Los Angeles, California, *Geophys. Res. Lett.,* **31,** L23613.

Larsen, C., Motyka, R., Freymueller, J. K. A. E. & Ivins, E., 2005. Rapid viscoelastic uplift in southeast Alaska caused by post-Little Ice Age glacial retreat, *Earth planet. Sci. Lett.,* **237,** 548–560.

Li, Z., Muller, J.-P., Cross, P. & Fielding, E.J., 2005. Interferometric synthetic aperture radar (InSAR) atmospheric correction: GPS, Moderate Resolution Imaging Spectroradiometer (MODIS), and InSAR integration, *J. geophys. Res.,*B03410.

Li, Z., Muller, J.-P., Cross, P., Albert, P., Fischer, P. & Bennartz, R., 2006. Assessment of the potential of MERIS near-infrared water vapour products to correct ASAR interferometric measurements, *Int. J. Rem. Sens.,* **27,** 349–365.

Lyons, S. & Sandwell, D., 2003. Fault creep along the southern San Andreas from InSAR, permanent scatterers, and stacking, *J. geophys. Res.,* **108,** 2047.

Ma, C., Sauber, J., Bell, L., Clark, T., Gordon, D., Himwich, W. & Ryan, J.W., 1990. Measurement of horizontal motions in Alaska using very long baseline interferometry, *J. geophys. Res.,* **95,** 21 991–22 011.

Matmon, A., Schwartz, D., Haeussler, P., Finkel, R., Lienkaemper, J., Stenner, H. & Dawson, T., 2006. Denali Fault slip rates and Holocene-late Pleistocene kinematics of central Alaska., *Geology,* **34,** 645–648.

Meriaux, A.-S., Sieh, K., Ryerson, F.-J., Finkel, R., Taylor, M., M., R.C. & Meltzner, A., 2004. Kinematics of the southern Alaska constrained by westward-decreasing post-glacial slip-rates on the Denali fault, Alaska, *EOS, Trans. Am. geophys. Un.*, Fall Meeting Suppl., Abstract G13C–07.

Page, R. & Lahr, J., 1971. Measurements for fault slip on the Denali, Fairweather and Castle Mountain Faults, *J. geophys. Res.,* **76,** 8534–8543.

Parsons, B., Wright, T.J., Rowe, P., Andrews, J., Jackson, J., Walker, R., Khatib, M. & Talebian, M., 2006. The 1994 Sefiadbeh (eastern Iran) earthquakes revisited: new evidence from satellite radar interferometry and carbonate dating about the growth of an active fold above a blind thrust fault, *Geophys. J. Int.,* **164,** 202–217.

Peltzer, G., Crampe, F., Hensley, S. & Rosen, P., 2001. Transient strain accumulation and fault interaction in the Eastern California shear zone, *Geology,* **21,** 975–978.

Plafker, G., Gilpin, L. & Lahr, J., 1994. Neotectonic Map of Alaska, in *The geology of North America,* eds Plafker, G. & Berg, H.C., Geol. Soc. Am, Boulder, Colorado.

Pollitz, F., Peltzer, G. & Burgmann, R., 2000. Mobility of continental mantle: Evidence from postseismic geodetic observations following the 1992 Landers earthquake, *J. geophys. Res.,* **105,** 8035–8054.

Prescott, W. & Nur, A., 1981. The accommodation of relative motion at depth on the San Andreas Fault System in California, *J. geophys. Res.,* **88,** 1217–1230.

Pritchard, M. & Simons, M., 2002. A satellite geodetic survey of large-scale deformation of volcanic centres in the central Andes., *Nature,* **418,** 167–171.

Ratchkovski, N., Wiemer, S. & Hansen, R., 2004. Seismotectonics of the central Denali Fault, Alaska and the 2002 Denali Fault earthquake sequence, *Bull. seism. Soc. Am.,* **64,** 156–174.

Rignot, E., 1998. Fast Recession of a West Antarctic Glacier, *Science,* **281,** 549–551.

Rosen, P., Hensley, S., Peltzer, G. & Simons, M., 2004. Updated Repeat Orbit Interferometry package released, *EOS, Trans. Am. geophys. Un.,* **85,** 35.

Savage, J., 1990. Equivalent strike-slip earthquake cycles in half space and lithospheric-asthenosphere earth models, *J. geophys. Res.,* **95,** 4873–4879.

Savage, J. & Burford, R., 1973. Geodetic determination of relative plate motion in California., *J. geophys. Res.,* **78,** 832–845.

Savage, J.C. & Lisowski, M., 1991. Strain Accumulation along the Denali fault at the Nenana river and Delta river crossings, *J. geophys. Res.,* **96,** 14 481–14 492.

Scharoo, R. & Visser, P., 1998. Precise orbit determination and gravity field improvement for the ERS satellites, *J. geophys. Res.,* **103,** 8113–8127.

Schmidt, D.A. & Burgman, R., 2003. Time-dependent land uplift and subsidence in the Santa Clara valley, California, from a large interferometric, synthetic aperture radar dataset, *J. geophys. Res.,* **108,** 8534–8543.

Segall, P., 2002. Integrating geologic and geodetic estimates of slip rate on the San Andreas fault system, *International Geology Review,* **44,** 62–82.

Stout, J. & Chase, C., 1980. Plate Kinematics of the Denali Fault system, *Can. J. Earth Sci.,* **17,** 1527–1537.

Stout, J., Brady, J., Weber, F. & Page, R., 1973. Evidence for Quaternary Movement on the McKinley Strand of the Denali Fault in the Delta River area, Alaska, *Geol. soc. Am. Bull.,* **84,** 939–948.

Wadge, G. *et al.*, 2002. Atmospheric models, GPS and InSAR measurements of the tropospheric water vapour field over Mount Etna, *Geophys. Res. Lett.,* **29,** 1905.

Wesson, R., 1988. Dynamics of Fault Creep, *J. geophys. Res.,* **83,** 8929–8951.

Wright, T., Parsons, B. & Fielding, E., 2001. Measurement of interseismic strain accumulation across the North Anatolian Fault by satellite radar interferometry, *Geophys. Res. Lett.,* **28**(6), 2117–2120.

Wright, T., Lu, Z. & Wicks, C., 2004a. Constraining the Slip Distribution and Fault Geometry of the Mw7.9, 2 November 2002, Denali Fault Earthquake with Interferometric Synthetic Aperture Radar and Global Positioning System Data, *Bull. seism. Soc. Am.,* **94**(6B), S175–S189.

Wright, T., Parsons, B., England, P. & Fielding, E., 2004b. InSAR observations of low slip rates on the major faults of western Tibet, *Science,* **305,** 236–239.

Zebker, H., Rosen, P. & Goldstein, R.M., 1994. On the derivation of coseismic displacement fields using differential radar interferometry: The Landers earthquake, *J. geophys. Res.,* **99,** 19 617–19 634.

Ziebart, M., Adhya, S., Sibthorpe, A., Edwards, S. & Cross, P., 2005. Combined radiation pressure and thermal modelling of complex satellites: Algorithms and on-orbit tests, *Adv. Space Res.,* **36,** 424–430.

SUPPLEMENTARY MATERIAL

The following supplementary material is available for this article:

Appendix S1. One table and three supplementary figures are in this supplementary appendix.

This material is available as part of the online article from:

http://www.blackwell-synergy.com/doi/abs/10.1111/j.1365-246X.2007.03415.x

(this link will take you to the article abstract).

Please note: Blackwell Publishing are not responsible for the content or functionality of any supplementary materials supplied by the authors. Any queries (other than missing material) should be directed to the corresponding author for the article.